Improved Wavelet Threshold Transform for SAR Image Oil Spill Detection

Siyuan Chen, Xueyun Wei and Wei Zheng

August 11, 2022

Improved Wavelet Threshold Transform for SAR Image Oil Spill Detection

Siyuan Chen[1]*, **Xueyun Wei**[2], **Wei Zheng**[3]

[1]Ocean College, Jiangsu University of Science and Technology, Zhenjiang Jiangsu 212100, China
[2]Ocean College , Jiangsu University of Science and Technology, Zhenjiang Jiangsu 212100, China
[3]Ocean College , Jiangsu University of Science and Technology, Zhenjiang Jiangsu 212100, China
*E-mail:310186136@qq.com

Abstract: Big data shows that offshore oil spills have been on the rise in recent years. Oil spills at sea can be monitored using SAR images, which can assist in preventing the economic damage and pollution caused by spills. Detecting offshore oil spills with SAR images is essentially a segmentation of oil spill images. However, reliably distinguishing the oil spill location from the clean sea surface area using SAR photos is a huge challenge. Considering that the SAR image itself has multiplicative noise, the traditional threshold segmentation algorithm has many defects. To overcome this challenge, methods based on a wavelet threshold transform and the Otsu segmentation algorithm were applied. Therefore, this study is devoted to enhancing the denoising effect of wavelet threshold transform, so as to further improve the segmentation accuracy of oil spill area and clean sea area. In this study, a new hierarchical adaptive threshold and a threshold function with bi-directional shrinkage are proposed to handle wavelet coefficients. While removing the SAR image noise, the edge details of the oil spill area can be retained. Experiments demonstrate that the suggested strategy enhances overall denoising and segmentation accuracy significantly.

Keywords: SAR; oil spill detection; image segmentation; wavelet threshold transformation; threshold function

1. Introduction

Ocean oil spills have become a serious environmental and public economic security concern that cannot be overlooked. The maritime transportation business and offshore oil and gas sector have grown quickly in the latest few years in virtue of growing concern about the exploitation of marine resources [1,2]. Oil spills from ships and offshore oil rigs, on the other hand, occur often in various waterways across the world, wreaking havoc on the environment and destroying property. More than $1 billion was allegedly spent and over two hundred thousand marine creatures were evaporated noiselessly in Deep Water Horizon oil leak in 2010 [3]. The growing quantity of marine oil spill contaminants will have a severe influence on the environment, biodiversity will decline, and ecological imbalance would eventually jeopardise human existence and progress. Therefore, distinguishing oil spill areas from clean sea surface areas from SAR oil spill images is a major challenge.

There are currently two basic methods for locating an oil leakage district: manual abstraction and automated abstraction. The trend, edge texture, form, and other interpretation cues of the oil spill region characteristics in SAR pictures are commonly employed to identify clean seawater from the oil spill area [4,5]. This is a manual extraction procedure. However, on this account, visual decipherment necessitates picture decipherment, the reader must have extensive expertise with visual decipherment as well as a thorough understanding of many earth scientific concepts, which necessitates additional effort. Furthermore, this method of interpretation is labor-intensive, and it is strenuous to guarantee the quality of interpreted photographs to a degree. Because oil spills occur so often, precise, efficient, and automated offshore oil spill monitoring has become a need. As a result, present SAR image oil spill region extraction research is mostly focused on automated extraction [6,7].

Extracting the oil spill zone from SAR images is a technique of image division on the basis of features of seawater and oil film border. Threshold segmentation algorithms are the most used picture segmentation methods (e. g. Otsu algorithm, maximum entropy algorithm). Although these threshold segmentation methods are uncomplicated and quick, they are susceptible to noise, and the edge localization is insufficient, therefore they are not universally applicable. Many researchers have conducted active exploration and developed various successful extraction techniques in order to discover the entire and accurate oil spill zone from SAR images.

Wavelet Threshold Transform (WTT) is developed on the basis of spatial filtering algorithm. The two-dimensional discrete wavelet threshold transform is a huge accomplishment in image denoising and has a lot of research potential. In recent years, with the extensive research on wavelet threshold transform denoising algorithm, two-dimensional discrete wavelet threshold transform denoising algorithm has been widely concerned by researchers and involved in more and more fields. However, due to the problems of blurred boundary, low contrast, high gray scale and susceptibility to noise interference in SAR images, the traditional method of 2D discrete wavelet threshold transform still encounters some problems, such as weak edge information, image distortion and small granular noise cannot be removed.

From this paper, this enhanced wavelet threshold transform is presented to increase the denoising impact on oil spill photos, and it is integrated with the Otsu threshold segmentation

technique to further improve the segmentation accuracy of the offshore oil spill region. This paper first proposes a novel hierarchical adaptive thresholding estimation formula, which fully considers the relative changes of image signal and noise coefficients at each wavelet scale and better fits the distribution of speckle noise in each layer. Then a novel threshold function with two-way preserving shrinkage is proposed, and an adjustment factor is introduced to eliminate the noise coefficients while protecting the oil spill region edge detail coefficients, making denoised images more realistic. Finally, the Otsu algorithm is used to threshold the denoised image for segmentation. By comparing two picture quality evaluation index, the enhanced approach in this study is compared to the classic wavelet threshold transform method, and then the segmentation result map using the OTSU algorithm and the segmentation result map of the oil spill image decoded by experts are compared precisely element by element to derive the segmentation accuracy, which further illustrates the applicability of the method in this paper and the great prospect of application in SAR image oil spill detection.

This is the layout of the paper. The background and associated research are presented in Section 2, as well as the major approaches of wavelet threshold transform for SAR picture denoising. In this work, Section 3 covers the materials and techniques, which include the research data, the traditional wavelet threshold transformation, the wavelet threshold transform enhancement, and the oil spill region extraction method. In Section 4 , the features of the improved threshold function are validated. In Section 5, these findings of the experiments are organized . Finally, in Section 6, these findings and potential study directions are reviewed.

2. Background and Related Work:

The most widely utilized and efficient monitoring approach is oil spill detection using SAR images [4]. Imaging geometry is an oblique projection type in an active side facing radar system [5]. The back scattering of a signal is affected by the working wavelength, incidence angle, polarization mode, superficies rugosity, and dielectric constant of the ground substance of a radar sensor [6]. Accidents involving oil spills are common in locations with complicated maritime ecosystems[7]. As a result, entering the contaminated region to liquidate or take stock in the early stages is difficult. Such occurrences typically last days [8, weeks [9], or even months [10], necessitating ongoing monitoring to better understand how oil spills spread [11]. Different polarization phenomena are formed by the horizontal and vertical polarization electric field vectors. Rough surfaces have a higher back scattering intensity than smooth surfaces. Because the oil spill region's surface is significantly smoother than seawater's without evident wave effect, the oil spill region appears as black pixels in the synthetic aperture radar picture, whereas the saltwater surface appears as brilliant pixels [12].

Substantial studies have been conducted in order to extract image information from SAR images. In these studies, four main types of methods have been applied. Filtering methods include linear, nonlinear, partial differential equation (PDE), and discrete wavelet transform (DWT)-based filtering.

Mean filter, Gaussian filter, box filter, Laplace filter, and other linear filters are common. The stencil coefficient is usually the sole variation between linear filters. The mean filtering technique selects the current pixel to be processed as a template, which is made up of a number of pixels in its vicinity, and uses the template's mean value to replace the value of the

original pixel. The technique lowers noise by blurring the image, notably the edges and features of the scene, yet being simple and computationally quick. It is very sensitive to noisy images, especially those with large isolated points, and even a very small number of points with large differences can lead to significant fluctuations in the average value. The mean filter performs poorly in terms of edge protection because it ignores the image's flat and homogenous areas [13].Gaussian filtering is effective at reducing noise that is introduced randomly at the picture input and typically targets Gaussian noise. It works by considering pixel points as a Gaussian distribution in respect to neighboring pixels and convolving the picture using a Gaussian kernel. The usual reason for performing Gaussian filtering is that real images vary slowly in space in terms of pixels, so that pixel changes in close proximity will not be significant, but two random points may form a large pixel difference. It is on this basis that Gaussian filtering reduces noise while preserving the signal. Unfortunately, this method becomes ineffective close to the edges, so Gaussian filtering destroys image edges.

Non-linear filtering, such as median filters, bilateral filters (BF) [13], and non-local average filters (NLM) [14], rely on a logical link between the original picture and the template to produce the desired output. These filtering algorithms keep the image's edge areas while removing noise. The median filtering technique involves choosing a template for the current pixel to be processed, which consists of a number of pixels in its vicinity, sorting the pixels of the template from smallest to biggest, and replacing the original pixel's value with the template's median value. As a result, in homogenous regions, this median filtering approach performs well at denoising. However, it does poorly towards the periphery in terms of retention. Bilateral filtering constructs a weighted average based on each pixel and its domain, and the weighting calculation consists of two parts, where the first part is weighted in the same way as Gaussian filtering, and the second part is also part of Gaussian filtering weighting, but instead of weighting which is on basis of the spatial distance between the central pixel point and the other pixel points above, it is weighted based on the difference in luminance between the other pixels and the central pixel. As a result, this approach performs badly in terms of decreasing speckle noise since it is based on the Gaussian filtering concept. The NLM is a approach based on BF [15] that enhances performance. The similarity between pixel units is used by BF to apply weights. On the other side, the NLM filter is expanded to apply weights depending on the masks' similarity. While the previous ones averaged the local picture inside the neighborhood, NLM's noise reduction filtering procedure employs the information from the entire image. The main distinction between NLM and bilateral filtering is that bilateral filtering only calculates weights using the current and reference points, but NLM uses all values in the neighborhood. A sequence of actions on the picture block create the overall blurring of the output image. As a result, the NLM filter performs poorly in terms of diminishing speckle noise [16].

PDE approach is based on the notion of treating image processing as a process of solving partial differential equations. Using PDEs, the PDE approach turns noisy photos into PDEs, resulting in noise-free images [17]. Other noise reduction approaches include PDE-based filtering methods such as AD filters [18] and AWAD methods [19]. The gradient operator is employed in the AD filtering method to identify gradient fluctuations in the picture produced by noise and edge effects. Small gradient fluctuations produced by noise are removed by the closest neighbour weighted average approach, while big gradient variations induced by

edges are kept [20]. This AD filter approach has shown to be effective in smoothing additive noise in photographs. However, on this account, the noise in the speckle images cannot be identified by the AD filter, it has poor speckle noise (multiplicative noise) reduction performance. The mask's size and orientation are modified on the basis of image's structure. The AWAD approach may regulate the window's size and orientation, resulting in effective edge protection [21].

DWT approaches may examine the signal's localisation in terms of time and frequency[22]. Because of its useful qualities, DWT has been widely employed in different image processing disciplines since the 1990s and is progressively becoming one of the most researched approaches [23].The DWT method for speckle noise removal has the following steps. DWT [24] is used to do a multiscale decomposition of the picture first. Following that, wavelet functions are used to minimize unwanted wavelet coefficients [25]. Hard threshold [26], soft threshold [27], and universal threshold [28] are examples of traditional threshold approaches. Finally, the processed wavelet coefficients are synthesized into a noise-free image by inverse DWT [29]. The conventional DWT method can effectively remove the noises with larger particles, however those with smaller particles cannot be removed. The DWT method based on the thresholding method and wavelet function can lead to blurred edges of images, which   have affect on the final segmentation accuracy because traditional threshold method and wavelet function have great defects [30].

3. Materials and methods:

3.1. Data

The data used in this paper are from four full polarization SAR images of radarsat-2 and the corresponding expert interpretation results of the oil spill area. As shown below, the first and fourth photographs of an oil spill in Beihai, Europe, in June 2011 were interpreted as three substances (crude oil, oil emulsion, vegetable oil). The second and third photos were taken in May 2010 and August 2011 respectively.
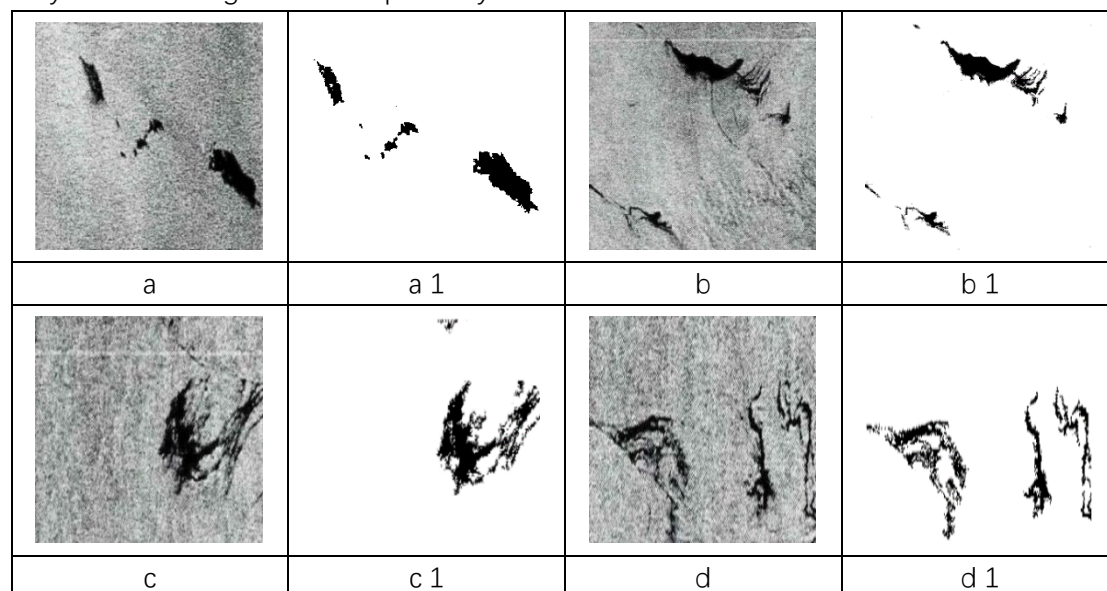

a	a 1	b	b 1

c	c 1	d	d 1

Fig. 1 SAR image and the result image of oil spill expert interpretation. **(a-d)** fully polarized SAR images, **(a1-d1)** the result images interpreted by oil spill experts corresponding to the SAR image

3.2. Theoretical Background

3.2.1. Logarithmic Transformation

The model is worsened by speckle noise in SAR pictures, as shown in Equation (1)[31].

$$P(a,b) = U(a,b) \times Q(a,b) + C(a,b) \qquad (1)$$

Where $P(a,b)$ is the SAR picture's degraded image. The original picture is $U(a,b)$, speckle noise is $Q(a,b)$, and additive noise is $C(a,b)$ [33]. Because additive noise has a smaller impact on SAR pictures, it is usually excluded, and Equation (2) is found.

$$P(a,b) = U(a,b) \times Q(a,b) \qquad (2)$$

It is pretty strenuous to distinguish actual picture from whole degraded image when a multiplicative noise model is used to represent speckle noise. In terms of the logarithmic transformation, the speckle noise becomes additive noise, as shown in equation (2)[32]:

$$\log P(a,b) = \log U(a,b) + \log Q(a,b) = M(a,b) + S(a,b) \qquad (3)$$

$$F(a,b) = M(a,b) + S(a,b) \qquad (4)$$

The logarithms of $P(a,b)$, $U(a,b)$, and $Q(a,b)$ are $F(a,b)$, $M(a,b)$, and $S(a,b)$, respectively ,and we try to eliminate noise in the wavelet domain.

3.2.2. Discrete wavelet decomposition of SAR image

The core principle of the DWT is explained as follows for the 2D picture. A SAR image is transformed into four sub-band images using one-level DWT (Fig 2b) which are consists of approximation sub-band picture and three high-frequency sub-band pictures. The results of the two-level wavelet decomposition [34] are shown in Fig 2c. The two-level DWT decomposes the LL1 sub-band picture to produce four sub-band images. The low-frequency coefficients are represented by the approximate sub-band image (LL2), while the high-frequency coefficients are represented by detailed sub-band images. The lower frequency sub-band images contain detailed information about the image, which consists of texture and edge information. Whereas noise is contained in the sub-band images at high frequencies [35].
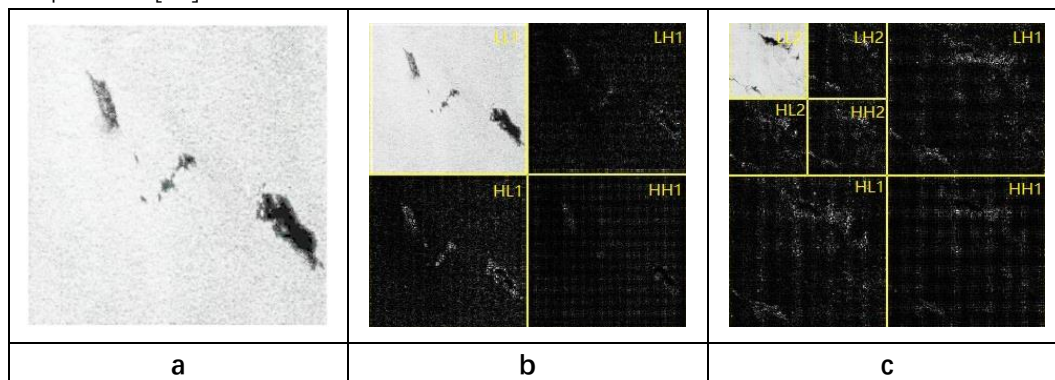

Fig. 2 The two-dimensional image decomposition results under different discrete wavelet transform scales. (**a**) the preprocessed oil spill image, (**b**) the image under one-layer wavelet decomposition, (**c**) the image under two-layer wavelet decomposition

3.2.3. Traditional threshold λ Estimation formula

Visushrink threshold uses the same threshold in each sub-band image of wavelet. [36]This method is also called "unified threshold method". In wavelet threshold denoising, because the amplitude change of noise coefficient is small and the number is huge, the wavelet coefficients larger than Visushrink threshold tend to zero after wavelet decomposition

[37]. The estimation method is expressed as follows:

$$\lambda = \sigma\sqrt{2\log N} \tag{5}$$

Where, σ represents the noise standard deviation, N corresponds to the length of the signal after wavelet transform. Wavelet performs a multi-scale transform, and as decomposition scale increases, amplitude of useful signal of the image will become larger and larger, and the number of image signals and noise signals in different wavelet layers will be different, and VisuShrink threshold uses a uniform threshold for wavelet coefficients at different scales. In this way, some useful signal coefficients in the image are easily filtered out, which affects the denoising effect[38].

3.2.4. Improved threshold λ Estimation formula

For the shortages of VisuShrink threshold, this paper proposes a hierarchical adaptive threshold[39], as shown in the following equation:

$$\lambda = \sigma\sqrt{2\log N} / \log(1 + e^{1-\frac{1}{j}}) \tag{6}$$

Like the Visushrink threshold, σ Represents the standard deviation of noise images, N is the length of the signal after wavelet transform, j represents the decomposition scale, and when J is equal to 1, it is the Visushrink threshold. When wavelet decomposition, the image signal amplitude and noise amplitude change in opposite directions as the scale j increases, and the threshold λ becomes smaller accordingly. Compared with the VisuShrink threshold, the new threshold fully takes into account the relative changes of image signal and noise coefficients at each wavelet scale, and is more consistent with the distribution of speckle noise in each layer[40].

3.2.5. Traditional threshold function

There are several threshold approaches [41-42]. The soft threshold and hard threshold wavelet functions are utilized wavelet functions. In SAR images, threshold approaches are used to eliminate speckle noise. When coefficients are less than these thresholds, both thresholds are set to zero, but there is a significant difference between them. The former suppresses coefficients greater than the threshold, whereas the latter keeps them constant[43].

3.2.5.1. Hard threshold function

The hard threshold eliminates the coefficients below the noise variance-determined threshold λ [44]. The following is a description of the hard threshold:

$$\widehat{W}_{j,k} = \begin{cases} W_{j,k}, & |W_{j,k}| \geq \lambda \\ 0, & |W_{j,k}| < \lambda \end{cases} \tag{7}$$

The wavelet coefficient is $W_{j,k}$, and the threshold is λ . After applying a hard threshold, the wavelet coefficients are represented as $W_{j,k}$. In noiseless pictures, the hard threshold is known to be discontinuous. because at the threshold value, the wavelet coefficients abruptly become 0 .The wavelet coefficients that do not surpass a specific threshold are canceled out in hard threshold approach, while the other wavelet coefficients remain unaffected. As a result, the despeckled image has artifacts due to the hard threshold[45].

3.2.5.2. Soft threshold function

To circumvent the issues of hard threshold, soft threshold uses symbolic functions in its model[46]. As seen in the formula below:

$$\widehat{W}_{j,k} = \begin{cases} sign(W_{j,k})(|W_{j,k} - \lambda|), & |W_{j,k}| \geq \lambda \\ 0 & , |W_{j,k}| < \lambda \end{cases} \qquad (8)$$

The symbolic role of the $sign$ is depicted here. The wavelet coefficients after scaling down the soft threshold are $\widehat{W}_{j,k}$. Wavelet coefficients are 0 in the soft threshold approach if they are below the threshold. The threshold reduces the scale of wavelet coefficients above it. As a result, gentle thresholding produces smooth, artifact-free output. Soft threshold typically has better preservation than hard threshold. Soft thresholding often preserves detail well at the cost of increased computing complexity. The image is blurred as a whole when using the soft threshold approach[47-48].

3.2.6. Improved threshold function

In order to solve the shortcomings of hard and soft threshold, this paper puts forward the following four requirements for the newly constructed threshold function:

(1) The threshold function should be continuous at the threshold to avoid additional oscillation of the denoised image or signal;

(2) The threshold function should take F (x) = x as the asymptotic line and have a good approximation degree to avoid constant deviation like the soft threshold function;

(3) The threshold function should have a relatively good smooth transition zone near the threshold, that is, there should be a relatively good smooth transition zone between the dividing point of noise and signal, so that the signal will be closer to the natural signal;

(4) The threshold function should meet the differentiability in order to realize the adaptive learning of gradient algorithm.

In order to meet the above four principles, this paper introduces the adjustment factor and constructs the new threshold function as follows:

$$\widehat{W}_{j,k} = \begin{cases} W_{j,k} + \dfrac{\lambda^{k+1}sign(W_{j,k})}{(m+1)|W_{j,k}|^k} - \dfrac{sign(W_{j,k})e^{m\lambda}}{e^{m|W_{j,k}|}}\lambda & , |W_{j,k}| \geq \lambda \\ \dfrac{sign(W_{j,k})|W_{j,k}|^{(m\lambda+1)(m+1)-k}}{(m+1)\lambda^{(m\lambda+1)(m+1)-(k+1)}} & , |W_{j,k}| \leq \lambda \end{cases} \qquad (9)$$

Where m and K are variable parameters with values between 0 and 1, and K is a positive integer. The threshold function which has been improved is adjustable and continuous in threshold point λ. The adjustment factors in the enhanced threshold function are the parameters m and K. The function has a hard threshold when k≥|λ| And m→0, and when 0<K<|λ| And m→1, the function is endlessly near to the soft threshold. At|$W_{j,k} \leq \lambda$| Smoothness in, m controls the change of wavelet coefficients, and K controls the threshold function. This research proposes a novel threshold function that combines the benefits of soft and hard thresholds. This paper's enhanced threshold function achieves a smooth transition of the wavelet threshold curve while avoiding the pseudo Gibbs phenomena.

3.3. Method

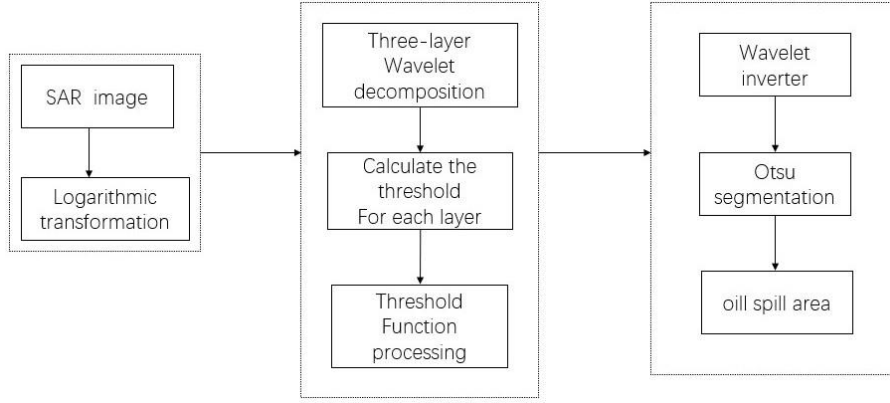3.3.1. Accurate extraction of oil spill area

Fig. 3 Extraction process of oil spill area

The following is the actual extraction procedure for the oil spill region.

Step 1: Perform a logarithmic transformation on the SAR picture.

Step 2: Using the revised threshold estimation algorithm, perform 3-layer 2D discrete wavelet decomposition on the pre-processed SAR picture and calculate the threshold value of each sub-band layer.

Step 3: The improved threshold function is used to process the wavelet coefficients of each layer, and the processed wavelet coefficients are synthesized into the denoised SAR picture using the inverse 2D discrete wavelet transform.

Step 4: Using the Otsu technique, threshold segment the denoised picture.

This method's flow chart is shown in Figure 3.

4.Verification

4.1. Continuity analysis

$$\lim_{x \to \lambda^-} f(x) = \frac{\lambda}{m+1}$$

$$\lim_{x \to \lambda^+} f(x) = \lambda + \frac{\lambda}{m+1} - \lambda = \frac{\lambda}{m+1}$$

That is, f (x) is in $x=\lambda$ Continuous at.

$$\lim_{x \to -\lambda^-} f(x) = \lambda - \frac{\lambda}{m+1} - \lambda = \frac{-\lambda}{m+1}$$

$$\lim_{x \to -\lambda^+} f(x) = \frac{-\lambda}{m+1}$$

That is, f (x) is in $x=-\lambda$ Continuous at.

4.2. Progressive analysis

$$\lim_{x \to +\infty} \frac{f(x)}{x} = \lim_{x \to +\infty} (1 + \frac{\lambda^{k+1}}{(m+1)|x|^{k+1}} - \frac{e^{m\lambda}}{e^{m|x|}x}\lambda) = 1$$

$$\lim_{x \to +\infty} \frac{f(x)}{x} = \lim_{x \to +\infty} (1 - \frac{\lambda^{k+1}}{(m+1)|x|^{k+1}} + \frac{e^{m\lambda}}{e^{m|x|}x}\lambda) = 1$$

4.3. Differentiability analysis

Because the function satisfies the differentiability, it is easy to realize complex mathematical calculation, and the number of parameters can be reduced by making the function satisfy the differentiability, which is convenient for subsequent simulation calculation. To satisfy the threshold function in the threshold variable λ It is differentiable at $x=\lambda$ It has continuity and differentiability at the threshold. Since the function has been continuous at the

threshold, to realize differentiability at the threshold, you need to meet:

$$\frac{\partial f(x)}{\partial \lambda}\big|_{x\to\lambda^-} = \frac{\partial f(x)}{\partial \lambda}\big|_{x\to\lambda^+}$$

Because:

$$\frac{\partial f(x)}{\partial \lambda}\big|_{x\to\lambda^-} = \frac{k+1}{m+1} - (m\lambda + 1)$$

$$\frac{\partial f(x)}{\partial \lambda}\big|_{x\to\lambda^+} = \frac{k+1}{m+1} - (m\lambda + 1)$$

So differentiability can be proved.

4.4. Threshold function image comparison

In order to facilitate observation and comparison, the threshold of each function in the figure is set to 5, the abscissa is $W_{j,k}$ and the ordinate is $\widehat{W}_{j,k}$. The function image of the new threshold function is a cluster function image in theory. In order to more clearly see the new threshold function image, the values of adjusting factor m and k in the above figure 4 are all 1.
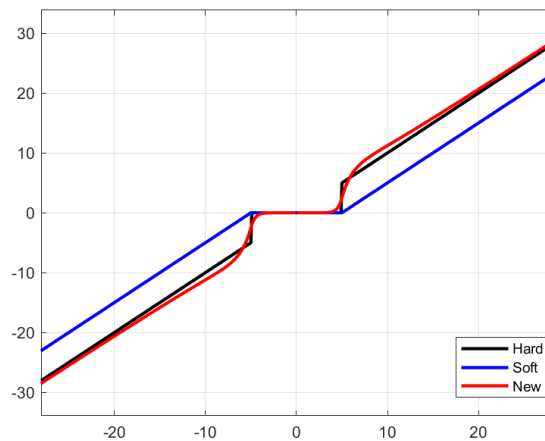

Fig. 4 Three threshold functions and images in the same coordinate system.

The hard threshold function is represented by the black solid line, the soft threshold function by the blue solid line, and the new threshold function by the red solid line, as illustrated in the diagram above. As shown in the diagram below, the threshold function suggested in this study not only has the benefit of being continuous at the threshold, but it also has the advantage of being more progressive than soft threshold function. The threshold function in this research features a gradual transition zone between thresholds, which is more similar to real signal characteristics.

5.Results

This section is mainly divided into three parts to show these results. The first part shows denoising effects of different denoising algorithms and improved wavelet threshold transform. The second part shows the evaluation index of denoised image. The third part is to accurately judge the denoised image and the oil spill image interpreted by experts pixel by pixel, and compare the segmentation accuracy.
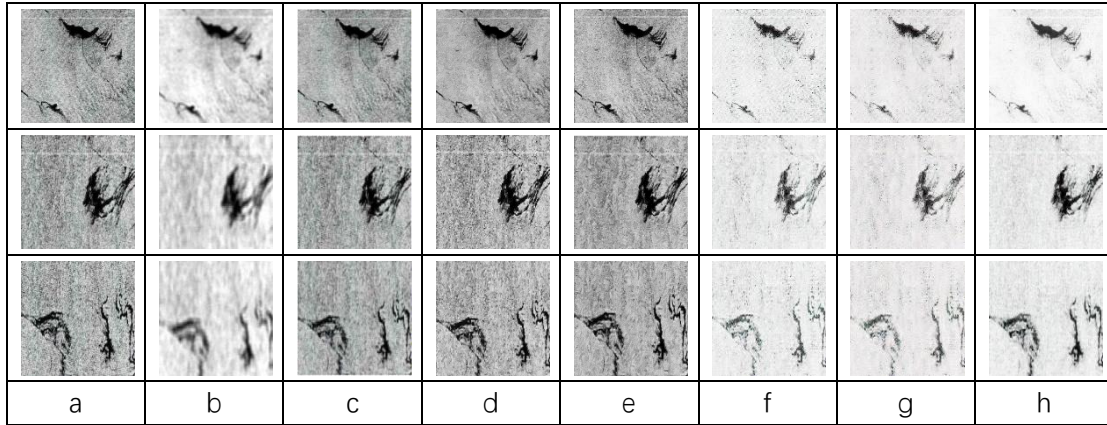
5.1. De-noised results
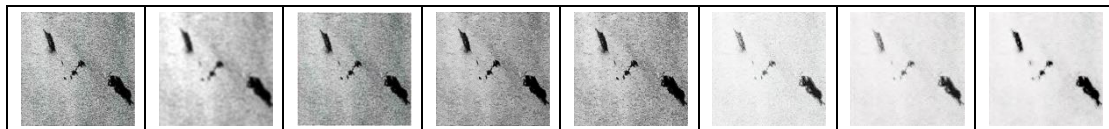
Figure 5. (a)SAR images, (b) Lee filter denoising images, (c)Frost filter denoising images, (d) NLM filter denoising images, (e) AWAD filter denoising images, (f) Hard threshold function denoising images, (g) Soft threshold function denoising images, (h) New threshold function denoising images.

5.2. Evaluation Metrics

MSE and PSNR are objective measuring tools for evaluating picture quality, with the following definition:

$$PSNR = 20\log_{10}(\frac{255}{\sqrt{MSE}}) \qquad (10)$$

$$MSE = \frac{1}{MN}\sum_{x=0}^{M-1}\sum_{y=0}^{N-1}\{Y(x,y) - Z(x,y)\}^2 \qquad (11)$$

The number of pixels in the vertical and horizontal directions of the picture are M and N, respectively. $Y(x,y)$ is the pixel value at the original image's position, and $Z(x,y)$ is the pixel value at the filtered image's coordinates. As the picture approaches the original image Y, the MSE of the filtered image $Z(x,y)$ decreases. The higher the PSNR number, the greater the noise reduction performance. SSIM is a similarity index that compares original picture $Y(x,y)$ with filtered image $Z(x,y)$. The following is SSIM:

$$SSIM(x,y) = \frac{(2\mu_x\mu_y + c_1)(2cov_{xy} + c_2)}{(\mu_x^2 + \mu_y^2 + c_1)(\sigma_x^2 + \sigma_y^2 + c_2)} \qquad (12)$$

The mean values of x and y are represented by μ_x and μ_y respectively. The variance of x and y is represented by the variables σ_x^2 and σ_y^2. The covariance of x and y is cov_{xy}. The variables c_1 and c_2 are utilised to stabilise the division that might arise when the denominator is weak[49-50].

Table1. MSE for SAR image

Noise variance	Lee	Frost	AWAD	NLM	Hard threshold	Soft threshold	Proposed
0.001	21.78	21.21	19.37	17.30	15.63	16.72	12.43
0.002	43.13	40.84	21.53	19.44	17.53	18.77	13.19
0.003	63.46	60.27	43.25	21.70	19.02	20.76	15.06
0.004	84.88	78.30	65.25	42.77	37.22	39.72	16.65
0.005	106.09	96.33	86.86	64.61	52.56	56.85	18.30
0.006	128.24	113.99	107.32	85.10	68.21	72.43	33.32
0.007	147.62	130.50	130.37	104.58	83.10	88.73	47.27
0.008	169.32	147.72	150.37	124.14	97.35	106.36	61.13

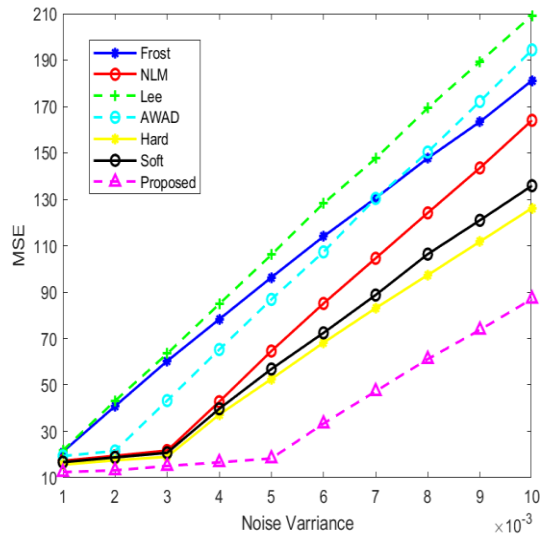| 0.009 | 189.25 | 163.39 | 172.14 | 143.51 | 111.77 | 120.95 | 73.72 |
| 0.01 | 219.20 | 181.19 | 194.38 | 164.04 | 126.24 | 135.86 | 87.09 |

Fig. 6 Plot of MSE versus noise variance for SAR image

Table2.PSNR values for SAR image

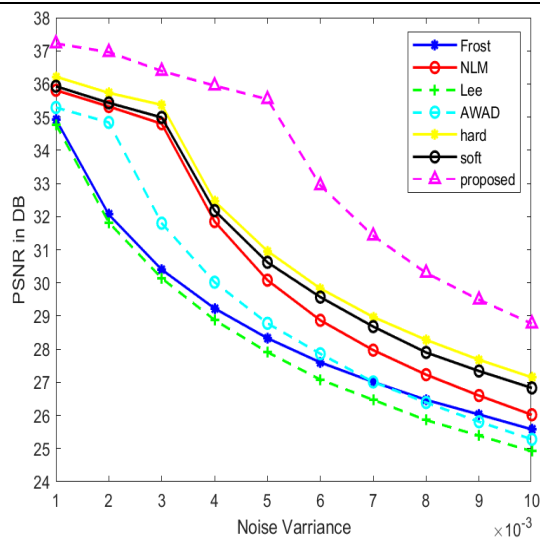| Noise variance	Lee	Frost	AWAD	NLM	Hard threshold	Soft threshold	Proposed
0.001	34.78	34.93	35.29	35.81	36.22	35.93	37.22
0.002	31.82	32.06	34.84	35.32	35.73	35.43	36.96
0.003	30.14	30.40	31.80	34.80	35.37	34.99	36.39
0.004	28.88	29.23	30.02	31.85	32.46	32.18	35.95
0.005	27.91	28.33	28.78	30.08	30.96	30.62	35.54
0.006	27.08	27.60	27.86	28.87	29.83	29.57	32.94
0.007	26.47	27.01	27.01	27.97	28.97	28.68	31.42
0.008	25.86	26.47	26.39	27.23	28.28	27.90	30.30
0.009	25.39	26.03	25.81	26.60	27.68	27.34	29.49
0.01	24.92	25.58	25.28	26.02	27.15	26.83	28.77

Fig. 7 Plot of PSNR versus noise variance for SAR image

Table3. SSIM for SAR image

Noise variance	Lee	Frost	AWAD	NLM	Hard threshold	Soft threshold	Proposed

| 0.001	0.770	0.675	0.798	0.841	0.896	0.873	0.950
0.002	0.690	0.624	0.748	0.836	0.782	0.783	0.931
0.003	0.654	0.576	0.725	0.833	0.719	0.762	0.904
0.004	0.637	0.532	0.714	0.831	0.678	0.754	0.895
0.005	0.629	0.493	0.707	0.829	0.651	0.750	0.887
0.006	0.624	0.457	0.703	0.828	0.632	0.748	0.882
0.007	0.621	0.425	0.700	0.826	0.619	0.747	0.877
0.008	0.619	0.396	0.698	0.824	0.609	0.746	0.875
0.009	0.617	0.371	0.696	0.821	0.603	0.745	0.874
0.01	0.616	0.349	0.695	0.819	0.598	0.744	0.873
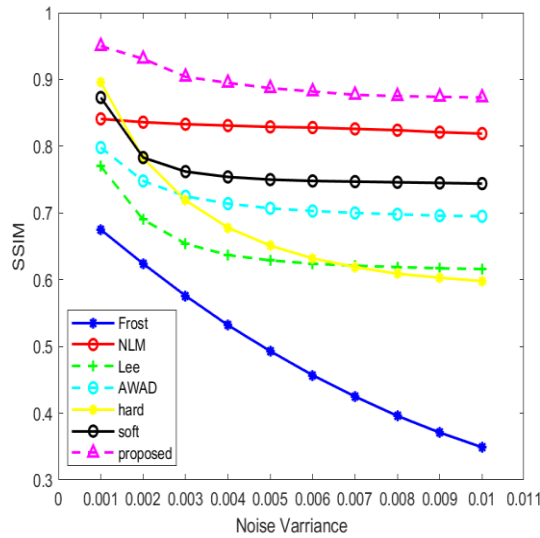
Fig. 8 Plot of SSIM versus noise variance for SAR image

In terms of MSE, PSNR, and SSIM, Figs. 6-8 compare the new approach to the previous technique. The suggested approach outperforms the present technique in terms of low and high noise, as shown in the figures. There is a significant reduction in MSE with different noise variances, and the PSNR and SSIM are improved accordingly.
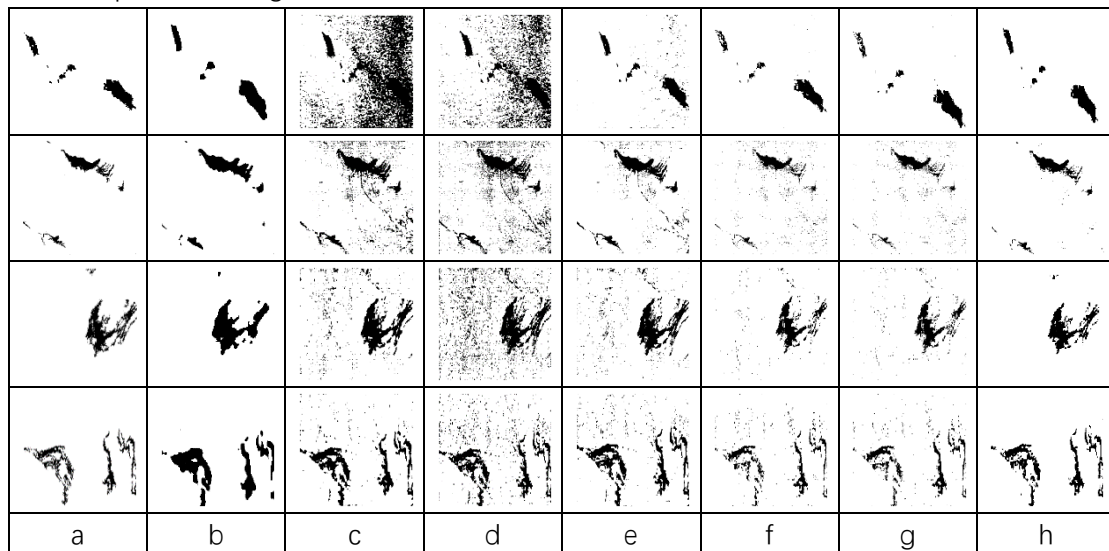
5.3. Comparison of segmentation results

Fig. 9 (a)Interpretation result images of oil spill expert, (b) Lee filter denoising segmentation

images, (c)Frost filter denoising segmentation images, (d) AWAD filter denoising segmentation images, (e) NLM filter denoising segmentation images, (f) Hard threshold function denoising segmentation images, (g) Soft threshold function denoising segmentation images, (h) New threshold function denoising segmentation images.

In this paper, Otsu algorithm is used to segment the image denoised by hard threshold function, soft threshold function and new threshold function respectively, and accurately judge the result image interpreted by oil spill experts pixel by pixel to obtain the segmentation accuracy. Through comparison, it can be found that the segmentation accuracy of images denoised by improved wavelet threshold transform is significantly higher than that of images denoised by traditional wavelet threshold transform. Therefore, it is reasonable to believe that the wavelet threshold transform has a great application prospect in SAR image oil spill detection. The division accuracy is shown in the following table:

Table 4. Accuracy results of each method in the proposed algorithm for each standard image

	Lee	Frost	AWAD	NLM	Hard threshold	Soft threshold	Proposed
Image 1	70.5%	65.4%	69.3%	82.3%	85.6%	87.2%	91.3%
Image 2	71.1%	77.4%	75.8%	85.6%	86.4%	88.4%	94.4%
Image 3	70.3%	76.3%	73.3%	83.4%	85.7%	86.3%	92.4%
Image 4	70.7%	79.8%	76.5%	82.1%	85.1%	86.7%	93.5%

6.Discussion and Conclusions

This study uses the improved wavelet threshold transform and Otsu segmentation algorithm to detect oil spill in SAR image. The traditional wavelet threshold transform has a good effect on removing the noise with large particles in SAR image, while the noise with small particles is difficult to remove, and the edge details of the image can not be well preserved, resulting in the blurring of the image edge after denoising, which affects the accuracy of segmentation. In view of the above research problems, this paper proposes a layered adaptive threshold and a new threshold function. The denoised image outperforms the standard wavelet threshold transform in terms of mean square error and peak signal-to-noise ratio, as demonstrated by testing on four full polarization SAR oil spill images, and the quality of the denoised image is guaranteed. The segmentation accuracy of the picture denoised by the enhanced wavelet threshold transform is much greater than that of the previous approach, according to the results of the image segmentation accuracy evaluation. For the remediation of maritime environmental contamination, accurate and prompt detection of oil spills is critical. Because the smooth surface and sea surface of the oil leaking location may produce variable performance of SAR image at sea, the most efficient technique to monitor offshore oil leakage is to utilize SAR image. The picture of the oil spill area, on the other hand, is comparable to that of similar oil spill areas, which is another essential aspect determining the accuracy of the oil spill area. Although the oil spill detection approach suggested in this research enhances segmentation accuracy by combining enhanced wavelet threshold transform and Otsu segmentation algorithm, it can only be used to extract oil spill dark spots and cannot determine the kind of oil film. Therefore, in the future research, we can continue to dig deeper and further combine convolutional neural network to classify oil film.

References

1. Beyer, J.; Trannum, H.C.; Bakke, T.; Hodson, P.V.; Collier, T.K. Environmental effects of the Deepwater Horizon oil spill: A review. Mar. Pollut. Bull. 2016, 110, 28–51. [CrossRef]

2.Smith, L.; Smith, M.; Ashcroft, P. Analysis of environmental and economic damages from British Petroleum's Deepwater Horizon oil spill. Albany Law Rev. 2011, 74, 563–585. [CrossRef]

3. Minchew, B.; Jones, C.E.; Holt, B. Polarimetric analysis of backscatter from the Deepwater Horizon oil spill using L-Band synthetic aperture radar. IEEE Trans. Geosci. Remote. Sens. 2012, 50, 3812–3830. [CrossRef]

4. Solberg, A.S.; Storvik, G.; Solberg, R.; Volden, E. Automatic detection of oil spills in ERS SAR images. IEEE Trans. Geosci. Remote. Sens. 1999, 37, 1916–1924. [CrossRef]

5. Schuler, D.; Lee, J.-S.; De Grandi, G. Measurement of topography using polarimetric SAR images. IEEE Trans. Geosci. Remote. Sens. 1996, 34, 1266–1277. [CrossRef]

6. Auer, S.J.; Hinz, S.; Bamler, R. Ray Tracing for Simulating Reflflection Phenomena in SAR Images. In Proceedings of the IGARSS 2008–2008 IEEE International Geoscience and Remote Sensing Symposium, Boston, MA, USA, 7–11 July 2008.

7. Gao, Q.; Lu, Y.; Sun, N.; Sun, Z.-L.; Zhang, D. Directionlet-based denoising of SAR images using a Cauchy model. Signal Process. 2013, 93, 1056–1063. [CrossRef]

8. Lan, G.; Li, Y.; Chen, P. Time Effffectiveness Analysis of Remote Sensing Monitoring of Oil Spill Emergencies: A Case Study of Oil Spill in the Dalian Xingang Port. Adv. Mar. Sci. 2012, 4, 13.

9. Yin, L.; Zhang, M.; Zhang, Y. The long-term prediction of the oil-contaminated water from the Sanchi collision in the East China Sea. Acta Oceanol. Sin. 2018, 37, 69–72. [CrossRef]

10. Yu, W.; Li, J.; Shao, Y. Remote sensing techniques for oil spill monitoring in offffshore oil and gas exploration and exploitation activities: Case study in Bohai Bay. Pet. Explor. Dev. 2007, 34, 378.

11. Qiao, F.; Wang, G.; Yin, L.; Zeng, K.; Zhang, Y.; Zhang, M.; Xiao, B.; Jiang, S.; Chen, H.; Chen, G. Modelling oil trajectories and potentially contaminated areas from the Sanchi oil spill. Sci. Total Environ. 2019, 685, 856–866. [CrossRef]

12. Keydel, W.; Alpers, W. Detection of oil fifilms by active and passive microwave sensors. Adv. Space Res. 1987, 7, 327–333. [CrossRef]

13. Tomasi, C.; Manduchi, R. Bilateral Filtering for Gray and Color Images. In Proceedings of the Sixth International Conference on Computer Vision, Bombay, India, 4–7 January 1998; pp. 839–846.

14. Buades, A.; Coll, B.; Morel, J.-M. A non-local algorithm for image denoising. In Proceedings of the 2005 IEEE Computer Society Conference on Computer Vision and Pattern Recognition, San Diego, CA, USA, 20–25 June 2005; pp. 60–65.

15. Buades, A.; Coll, B.; Morel, J.M. A review of image denoising algorithms, with a new one. SIAM Multiscale Model. Simul. 2005, 490–530. [CrossRef]Remote Sens. 2019, 11, 1184 26 of 27

16. Torres, L.; Sant'Anna, S.J.S.; Freitas, C.D.C.; Frery, C. Speckle reduction in polarimetric SAR imagery with stochastic distances and nonlocal means. Pattern Recognit. 2014, 141–157. [CrossRef]

17. Xu, W.; Tang, C.; Gu, F.; Cheng, J. Combination of oriented partial difffferential equation and shearlet transform for denoising in electronic speckle pattern interferometry fringe

patters. Appl. Opt. 2017, 56, 2843–2850. [CrossRef] [PubMed]

18. Perona, P.; Malik, J. Scale-Space and Edge Detection Using Anisotropic Diffffusion. IEEE Trans. Pattern Anal. Mach. Intell. 1990, 12, 629–639. [CrossRef]

19. Li, J.C.; Ma, Z.H.; Peng, Y.X.; Huang, H. Speckle reduction by image entropy anisotropic diffffusion. Acta Phys. Sin. 2013, 62, 099501.

20. Deledalle, C.A.; Denis, L.; Tupin, F. Iterative weighted maximum likelihood denoising with probabilistic patch-based weights. IEEE Trans. Image Process. 2009, 18, 2661–2672. [CrossRef]

21. Zhang, J.; Lin, G.; Wu, L.; Cheng, Y. Speckle filtering of medical ultrasonic images using wavelet and guided filter. Ultrasonics 2016, 65, 177–193. [CrossRef] [PubMed]

22. Su, X.; Deledalle, C.; Tupin, F.; Sun, F. Two-step multitemporal nonlocal means for synthetic aperture radar images. IEEE Trans. Geosci. Remote Sens. 2014, 52, 6181–6196.

23. Chierchia, C.; Mirelle, E.G.; Scarpa, G.; Verdoliva, L. Multitemporal SAR image despeckling based on block-matching and collaborative fifiltering. IEEE Trans. Geosci. Remote Sens. 2017, 55, 5467–5480. [CrossRef]

24. Parrilli, S.; Poderico, M.; Angelino, C.V.; Verdoliva, L. A nonlocal SAR image denoising algorithm based on LLMMSE wavelet shrinkage. IEEE Trans. Geosci. Remote Sens. 2012, 50, 606–616. [CrossRef]

25. Wu, M.-T. Wavelet transform based on Meyer algorithm for image edge and blocking artifact reduction. Inf. Sci. 2019, 474, 125–135. [CrossRef]

26. Singh, R.; Khare, A. Fusion of multimodal medical images using Daubechies complex wavelet transform—A multiresolution approach. Inform. Fusion 2014, 19, 49–60. [CrossRef]

27. Li, H.; Manjunath, B.S.; Mitra, S.K. Multisensor image fusion using the wavelet transform. Graph. Models Image Process. 1995, 57, 235–245. [CrossRef]

28. Pajares, G.; de la Cruz, J.M. A wavelet-based image fusion tutorial. Pattern Recognit. 2004, 37, 1855–1872. [CrossRef]

29. Huang, Z.-H.; Li, W.-J.; Wang, J.; Zhang, T. Face recognition based on pixel-level and feature-level fusion of the top-level's wavelet sub-bands. Inf. Fusion 2015, 22, 95–104. [CrossRef]

30. Hsia, C.-H.; Guo, J.-M. Effiffifficient modifified directional lifting-based discrete wavelet transform for moving object detection. Signal Process. 2014, 96, 138–152. [CrossRef]

31. Liu, S.; Florencio, D.; Li, W.; Zhao, Y.; Cook, C. A Fusion Framework for Camouflflaged Moving Foreground Detection in the Wavelet Domain. IEEE Trans. Image Process. 2018, 27, 3918–3930. [CrossRef]

32. Donoho, D.L. De-noising by soft-thresholding. IEEE Trans. Inf. Theory 1995, 25, 613–627. [CrossRef]

33. Donoho, D.L.; Johnstone, I.M. Adapting to unknown smoothness via wavelet shrinkage. J. Am. Stat. Assoc. 1995, 90, 1200–1224. [CrossRef]

34. Chang, S.G.; Yu, B.; Vetterli, M. Adaptive wavelet thresholding for image denoising and compression. IEEE Trans. Image Process. 2000, 9, 1532–1546. [CrossRef]

35. Yang, Y.; Ding, Z.; Liu, J.; Gao, Q.; Yuan, X.; Lu, X. An adaptive SAR image speckle noise algorithm based on wavelet transform and diffffusion equations for marine scenes. In Proceedings of the 2017 IEEE International Geoscience and Remote Sensing Symposium, Fort Worth, TX, USA, 23–28 July 2017; pp. 1–4.

[36] Bezdek, J.C., Ehrlich, R., Full, W.: 'FCM: The fuzzy c-means clustering algorithm', Comput.

Geosci., 1984, 10, (2–3), pp. 191–203

[37] Gao, X., Ji, H., Xie, W.: 'A novel FCM clustering algorithm for interval-valued data and fuzzy-valued data'. 2000 5th Int. Conf. on Signal ProcessingProc., WCCC-ICSP, 2000, pp. 1551–1555

[38] Tsantis, S., Spiliopoulos, S., Skouroliakou, A., et al.: 'Multiresolution edge detection using enhanced fuzzy c-means clustering for ultrasound image speckle reduction', Med. Phys., 2014, 41, (7), p. 072903

[39] Coifman, R.R., Meyer, Y., Quake, S., et al.: 'Signal processing and compression with wavelet packets' in 'Wavelets and their applications' (Springer, Berlin, 1994), pp. 363–379

[40] Cincotti, G., Loi, G., Pappalardo, M.: 'Frequency decomposition and compounding of ultrasound medical images with wavelet packets', IEEE Trans. Med. Imaging, 2001, 20, (8), pp. 764–771

[41]Bamberger, R.H., Smith, M.J.T.: 'A filter bank for the directional decomposition of images: theory and design', IEEE Trans. Signal Process.1992, 40, (4), pp. 882–893

[42] Do, M.N.: 'Directional multiresolution image representations'. PhD thesis, Swiss Federal Institute of Technology, Lausanne, Switzerland, 2001

[43] Vimalraj, C., Esakkirajan, S., Veerakumar, T., et al.: 'Direction sensitive wavelet packet for despeckling of ultrasound images', IET Comput. Vis.,2016, 10, (7), pp. 746–757

[44]Dunn, J.C.: 'A fuzzy relative of the ISODATA process and its use in detecting compact well-separated clusters', J. Cybern., 1973, 3, pp. 32–57

[45]Bezdek, J.C.: 'Pattern recognition with fuzzy objective function algorithms' (Plenum Press, New York, 1981)

[46] Krishnapuram, R., Keller, J.M.: 'The possibilistic c-means algorithm: insights and recommendations', IEEE Trans. Fuzzy Syst.., 1996, 4, (3), pp. 385–393

[47]Pal, N.R., Pal, K., Keller, J.M., et al.: 'A possibilistic fuzzy c-means clustering algorithm', IEEE Trans. Fuzzy Syst., 2005, 13, (4), pp. 517–530

[48]Song, I.S., Yoon, C.H., Kim, G.D., et al.: 'Adaptive frequency compounding for speckle reduction'. 2011 IEEE Int. Ultrasonics Symp., 2011, pp. 1435–1438

[49] Wang, Z., Bovik, A.C., Sheikh, H.R., et al.: 'Image quality assessment: from error visibility to structural similarity', IEEE Trans. Image Process., 2004, 13,(4), pp. 600–612

[50]Sheng, Y., Xia, Z.G.: 'A comprehensive evaluation of filters for radar speckle suppression'. Geoscience and Remote Sensing Symp., 1996, vol. 3, pp. 1559–1561